Optical properties and dielectric functions of grain boundaries and interfaces in CdTe thin-film solar cells

BG Mendis[1], QM Ramasse[2,3], TP Shalvey[4], JD Major[4] and K Durose[4]

1. Dept of Physics, Durham University, Durham, DH1 3LE, UK
2. SuperSTEM, SciTech Daresbury Campus, Daresbury, WA4 4AD, UK
3. School of Chemical and Process Engineering, University of Leeds, Leeds, LS2 9JT, UK
4. Stephenson Institute for Renewable Energy, Dept of Physics, University of Liverpool, Liverpool, L69 7ZF, UK

Abstract

CdTe thin-film solar cells have complex microstructures, such as grain boundaries within the absorber layer, as well as at the CdS window, or Au back contact interfaces. The local optical properties at these nano-scale defects are unknown, but are required in order to identify potential losses in device efficiency. Here monochromated electron energy loss spectroscopy (EELS) in an aberration corrected scanning transmission electron microscope (STEM) is used to measure the complex dielectric function for the $CdTe_{1-x}S_x$ inter-diffusion layer at the CdS-CdTe interface, high angle CdTe grain boundaries and Au-CdTe interface. $CdTe_{1-x}S_x$ is shown to have a lower absorption coefficient than CdTe, but its refractive index is more closely matched to CdS. Grain boundaries have a negligible effect on the light absorption profile within CdTe, despite significant changes in the local structure and chemistry (i.e. Te-depletion) at the grain boundary. Delocalisation in inelastic scattering is the dominant systematic error in the above measurements. Finally a light backscattering mechanism via surface plasmon polaritons at the Au-CdTe interface is uncovered, which could potentially increase the photocurrent extracted from incident light at energies just above the CdTe band gap.

Introduction

Thin-film solar cells, such as CdTe, utilise direct band gap semiconductors for efficient charge carrier generation through light absorption. The leading device materials, particularly CdTe, $Cu(In,Ga)Se_2$ and the hybrid perovskites, have in recent years exceeded 20% efficiency at the individual cell level [1], and are fast becoming commercially viable as alternatives to conventional silicon modules. In CdTe-based devices a recent innovation is to increase the short circuit current density (J_{sc}) by replacing the conventional CdS window layer with CdSe [2-4]. During device processing CdSe dissolves by inter-diffusion of Se into the CdTe absorber layer. The lower band gap of the $CdTe_xSe_{1-x}$ alloy results in stronger absorption of the long wavelength photons, while the simultaneous thinning of the CdSe window layer means that short wavelength photon losses are also minimised.

Sulphur from conventional CdS window layers is also known to inter-diffuse into the CdTe [5-6] and lower the band gap. The sulphur inter-diffused region is however narrower in comparison to the selenium equivalent, since the former is less soluble in CdTe [3]. External quantum efficiency (EQE) measurements indicate that there are photocurrent losses in the

~500-600 nm wavelength range for devices where sulphur inter-mixing is prevalent [7]. Quantification of photocurrent losses therefore requires determining the optical properties of the $CdTe_xS_{1-x}$ inter-diffusion layer in CdS-CdTe solar cells. This is however a challenging task since the sulphur diffusion profile shows a rapid decrease within only a few nanometres of the CdS-CdTe interface, followed by a broad, low sulphur concentration (i.e. few at%) tail extending ~500 nm into the CdTe [6]. Here monochromated electron energy loss spectroscopy (EELS) at high spatial resolution in an aberration corrected scanning transmission electron microscope (STEM) is used to probe the local optical properties of the inter-diffused layer [8]. By performing a Kramers-Kronig analysis of the EELS spectrum [9-10] the complex dielectric function, and hence optical properties, can be extracted, provided artefacts such as Cerenkov radiation [11] and delocalisation [12] are minimised or taken into account.

The optical properties of other interfaces in a CdTe device, such as grain boundaries and gold back contact, are also examined. Much of the interest on grain boundaries thus far has been on their role in non-radiative recombination and the resulting losses in V_{oc} [13-15]. Significant alteration of the structure and chemistry can take place at a grain boundary and hence a local variation in the optical properties is possible, which may also have an impact on device performance. For example, an increase in the optical absorption at the grain boundary means that a higher fraction of photo-generated charge carriers are potentially lost to non-radiative recombination. This is exacerbated by the fact that CdTe grains are columnar in structure [6], with grain boundaries extending through the film thickness. With high spatial and energy resolution EELS the role of CdTe grain boundaries on photo-carrier generation within the absorber layer can be evaluated for the first time. Furthermore, measurements for the gold back contact reveal a light backscattering mechanism via surface plasmon polaritons, which has the potential to increase the device photocurrent, especially at wavelengths close to the band gap of the absorber layer.

Experimental Method

For device fabrication 100 nm of CdS was radio frequency (RF) sputter deposited at 200ºC under 5 mTorr of argon on NSG Ltd TEC 15M glass. CdTe was subsequently close space sublimation (CSS) deposited after a substrate pre-anneal at 450ºC for 20 mins. The source and substrate temperatures during CSS deposition were 610º and 520ºC respectively. A two-stage deposition for 20 mins under 20 Torr of nitrogen followed by a 20 second vacuum deposition step at the same temperatures was used. The thickness of the CdTe absorber layer was ~2.5 μm. Samples were then etched in a nitric-phosphoric (NP) acid solution for 30 seconds [16] prior to a $MgCl_2$ activation step [17] for 30 mins at 410ºC in air. This was followed by a further NP etch for 15 seconds before thermal evaporation of a 50 nm thick gold back contact.

Cross-sections of the completed devices were thinned to electron transparency using an FEI Helios 600 focussed ion beam (FIB) microscope, with the final ion-beam voltage during thinning being 2 kV. The sample thickness was in the range of 25-45 nm, as determined by Kramers-Kronig analysis of EELS spectra (see below). Samples were examined in the Nion UltraSTEM 100 MC Hermes microscope at the SuperSTEM facility, Daresbury. Apart from the high spatial resolution due to the aberration corrected optics of the STEM column, this microscope is also capable of simultaneously achieving ~10 meV EELS energy resolution [8],

although in this work a dispersion of 20 meV/channel was used to acquire the low loss EELS spectra. Thus some energy resolution was sacrificed, limited by the point spread function of the detector, in order to increase the energy loss range (up to 37 eV) recorded in a single EELS spectrum; this is required in order to perform an accurate Kramers-Kronig analysis [18]. Chemical analysis was performed using core loss EELS with a dispersion of 0.3 eV/channel. The STEM probe semi-convergence angle was 31 mrad and the EELS collection semi-angle was 44 mrad. Images were simultaneously acquired using a medium angle annular dark field (MAADF) detector (55, 82 mrad inner and outer angles) as well as a high angle annular dark field (HAADF) detector (82, 180 mrad inner and outer angles). The operating voltage of the microscope was reduced to 60 kV in order to minimise Cerenkov radiation artefacts. Simulation of the electron energy loss function in the retarded and non-retarded regimes [19] using the dielectric properties for CdTe [20] showed that Cerenkov losses were negligible for the experimental conditions in this work. Kramers-Kronig analysis was performed using Gatan Digital Micrograph software. A combined Gaussian and Lorentzian model was used to fit the zero loss peak (ZLP) in the EELS spectra.

Results and Discussion

CdS_xTe_{1-x} inter-diffusion layer

Figure 1a shows a MAADF image of the CdS-CdTe interface with the CdS grain on the left hand side titled to the $[10\bar{1}0]$ zone-axis. In this orientation only the {111} lattice planes of zinc blende CdTe are resolved and these are rotated by 24° with respect to the (0002) planes in wurtzite CdS, as determined by the image Fourier transform. Furthermore, there is a ~11% lattice mismatch between the two phases, consistent with the lattice parameters reported for bulk crystals [21]. The mismatch strain is thought to be the origin of the white contrast at the interface in Figure 1a.

The EELS single scattering distribution for CdS, strained interfacial region and CdTe are shown superimposed in Figure 1b. The interfacial spectrum was acquired from the box region in Figure 1a, while the CdS and CdTe spectra were acquired approximately 15 nm into the respective bulk phase. The low loss EELS spectrum was Fourier-log deconvolved [9] in order to extract the single scattering distribution. The CdS spectrum thus obtained had some residual intensity from Cerenkov radiation, due to its larger band gap. This was removed by least squares fitting the spectrum to a function of the form $\alpha(E-E_g)^{½}$, where E is the energy loss and α, E_g are constants, over an energy window (i.e. 2.8-3.6 eV) above the band gap, extrapolating smoothly to E_g and setting all values below E_g to zero. The fitted function is based on the joint density of states for a direct band gap semiconductor with band gap E_g [22]. The E_g value obtained through this procedure was 2.34 eV, and is similar to the 2.41 eV band gap obtained from reflectance and transmittance measurements of micrometre thick CdS films [20].

The strained interfacial spectrum has characteristics of both bulk CdTe and CdS. For example, the fine structure peak ‘A’ is not as pronounced with respect to peaks ‘B’ and ‘C’, similar to CdS (Figure 1b; these peaks are due to interband transitions from the Cd 4*d* valence states [23]). On the other hand the band gap of the interfacial spectrum is closer to CdTe, though slightly red shifted (Figure 1b inset). It may be argued that the CdS-CdTe interface is not

atomically sharp and therefore the interfacial spectrum in Figure 1b contains contributions from both phases. To test this hypothesis the interfacial spectrum was multiple linear least squares (MLLS) fitted using three reference spectra, i.e. bulk CdTe and CdS spectra from Figure 1b as well as a delocalised spectrum, $\mathrm{Im}\{-2/(\varepsilon_{CdTe}+\varepsilon_{CdS})\}$, where 'Im' represent the imaginary part of a complex number, ε_{CdTe} is the dielectric function for CdTe, and similarly for ε_{CdS}. The delocalised spectrum represents the delocalised signal for an electron moving parallel to an interface between two bulk materials [24]. It is assumed that the incident electron trajectory is primarily parallel to the interface, although with interfacial roughness the incident electron can cross from one phase into another at certain depths within the specimen, and in these situations the delocalised signal will have a different mathematical form to that of a parallel trajectory [25]. The CdTe, CdS dielectric functions extracted from Kramers-Kronig analysis of the single scattering distributions in Figure 1b were used to calculate the delocalised spectrum. The result of the MLLS fitting procedure is shown in Figure 1c. Some prominent features of the spectrum, such as the fine structure peak 'A' at ~13 eV, are not accurately reproduced. Furthermore, the MLLS fitting coefficient for the delocalised spectrum was an unphysical negative value, while MLLS fitting carried out with only the bulk CdTe and CdS reference spectra produced a lower quality fit. This suggests that the interfacial spectrum measured at the strained layer is not governed primarily by CdS-CdTe interface roughness.

The S L- and Cd, Te M-edges were acquired using core loss EELS to explore any chemical origin to the interfacial low loss EELS signal, such as the sulphur diffusion reported previously for the CdS-CdTe interface [5-6]. Figure 1d shows the S to Cd (S:Cd) and Te to Cd (Te:Cd) intensity ratio profiles across the CdS-CdTe interface, extracted from the core loss EELS data, and superimposed with the simultaneously acquired MAADF signal. The intensities have been normalised for direct visual comparison. The S:Cd and Te:Cd intensity ratios vary over a distance of ~5.2 nm at the CdS-CdTe interface. This is too large to be due to beam broadening, since with the local specimen thickness measured to be ~45 nm, the geometric probe spreading for a 31 mrad STEM probe is only 1.4 nm. The fact that the atomic structure of CdS and CdTe are continuous right up to the interface (Figure 1a) also suggest that beam broadening and interfacial roughness are not significantly affecting the shape of the intensity ratio profiles. The most probable cause therefore appears to be sulphur diffusion and the formation of a $CdTe_xS_{1-x}$ interfacial layer. Red shifting of the interfacial spectrum band gap with respect to CdTe (Figure 1b inset) also supports this conclusion [20]. It should be noted however that the ~500 nm broad sulphur concentration tail of a few atomic% S reported in [6] is not observed here. This is attributed to differences in the measurement technique between the two studies. In reference [6] the sulphur concentration was measured using STEM energy dispersive X-ray (EDX) analysis with prolonged (i.e. 1 minute per data point) counting times, while in this study STEM EELS was used with an acquisition time of 0.4 s per data point. The lower peak-to-background and signal-to-noise ratio for EELS under the current experimental conditions makes it difficult to achieve sensitivities of a few atomic% for the S L-edge.

Before extracting optical properties for the $CdTe_xS_{1-x}$ interfacial layer it is necessary to discuss potential artefacts in the measurement. The first is that EELS involves finite collection angles, so that, strictly speaking, the results do not correspond to the 'optical limit', where the momentum transfer $q = 0$. Nevertheless there is strong evidence to suggest that the $q = 0$ contribution is dominant in the EELS spectra of Figure 1b. For example, momentum resolved

EELS has shown that a 2 mrad scattering angle is sufficient to suppress the doublet splitting of peak 'A' in the CdTe spectrum [23], although this feature is still clearly visible in Figure 1b. Furthermore, the CdTe fine structure peaks are known to show very little dispersion with respect to q, which is attributed to the strong interband contributions from the Cd 4d valence electrons [23]. Similar low loss EELS features in Figure 1b suggest that the same arguments may apply to CdS and the $CdTe_xS_{1-x}$ interfacial layer as well. A second and more serious measurement artefact applicable to the $CdTe_xS_{1-x}$ layer in particular is delocalisation in inelastic scattering [12]. To evaluate its effect the EELS low loss spectrum for a 2.8 nm $CdTe_xS_{1-x}$ layer sandwiched between bulk CdS and CdTe was simulated using the multilayer method described in [25-26]. The dielectric properties extracted from Kramers-Kronig analysis of the EELS spectra in Figure 1b were used in the simulation. A $CdTe_xS_{1-x}$ layer thickness of 2.8 nm was used since this corresponds to the Gaussian half-width of the composition profiles in Figure 1d. Further details of the simulation method can be found in the Supplementary Information. The simulated result is shown superimposed in Figure 1c. If delocalisation were negligible the simulated spectrum should be similar to the measurement. Examination of Figure 1c however shows that this is not the case; important differences are apparent, particularly at energy losses corresponding to visible and near-visible light, which is the operating conditions of a solar cell device. The optical properties of the $CdTe_xS_{1-x}$ interfacial layer reported here are therefore only approximate.

The low loss EELS spectra in Figure 1b for bulk CdTe and $CdTe_xS_{1-x}$ interfacial layer are Kramers-Kronig analysed to extract the real (ε_1) and imaginary (ε_2) parts of the complex dielectric function; these are shown in Figures 2a and 2b respectively. The dielectric function for CdTe is qualitatively similar to that measured using spectroscopic ellipsometry [27]. In particular, the E_0, E_1, $E_1+\Delta_1$ and E_2 direct optical transitions are identified in the ε_2 plot (Figure 2b; [27]). The first three optical transitions are suppressed at the interfacial layer, although E_2 is similar to bulk CdTe. This results in a lower absorption coefficient for the $CdTe_xS_{1-x}$ layer compared to CdTe over the solar spectrum wavelengths that are important for a solar cell device (Figure 2c). This is consistent with the results in [20], where apart from the $CdTe_{0.6}S_{0.4}$ composition, the absorption coefficient decreased on alloying CdTe with sulphur. The photocurrent generated in an absorber layer depends on the absorption coefficient as well as the reflectivity of light at the CdS window-absorber layer interface. A higher reflectivity means that less light is transmitted into the absorber layer, and consequently the photocurrent decreases. Figure 2d shows the reflectivity at normal light incidence for a CdS-CdTe interface as well as CdS-$CdTe_xS_{1-x}$, with the $CdTe_xS_{1-x}$ layer having the same dielectric properties as that displayed in Figures 2a and 2b. The reflectivity for CdS-$CdTe_xS_{1-x}$ is an improvement over the conventional CdS-CdTe interface, although the values for the latter are already close to ideal.

The combined effects of absorption coefficient and reflectivity on the photocurrent can be determined by calculating the external quantum efficiency (EQE) for devices with CdS window layer and either CdTe or $CdTe_xS_{1-x}$ absorber layer. Details of the calculation can be found in the Supplementary Information, but here it should be noted that the doping concentration for the two absorber layers is assumed to be identical (i.e. 10^{15} cm^{-3}), so that the space charge width in the 2.5 μm thick absorber layer is fixed at ~1.1 μm. The simulation of CdTe and $CdTe_xS_{1-x}$ absorber layers represents two extremes, since in a typical device the sulphur inter-diffused region will not extend through the entire absorber layer thickness. The EQE curves for the two

devices are shown superimposed in Figure 2e. The spike at 480 nm is an artefact arising from data processing to remove Cerenkov radiation in the CdS spectrum; it is due to the least squares fitted joint density of states function and experimental curves not having exact values at the point of extrapolation. There is a small increase in EQE in the plateau region for the $CdTe_xS_{1-x}$ absorber layer device; hence J_{sc} increases slightly from 18.1 to 18.3 mA/cm^2. The increase is due to the lower reflectivity of the CdS-$CdTe_xS_{1-x}$ interface, although its positive effects are partly negated by the lower absorption coefficient. Experimentally sulphur inter-mixing gives rise to a decrease in EQE in the ~500-600 nm wavelength range [7], although this is not observed in Figure 2e. This could be due to delocalisation errors in the extracted $CdTe_xS_{1-x}$ dielectric function, and/or other factors not taken into account in the EQE simulation, such as any effect of sulphur alloying on carrier diffusion length and space charge width, as well as the role of CdS-absorber layer misfit strain on carrier recombination [28].

CdTe grain boundaries

Figure 3a is a MAADF image of a CdTe high angle grain boundary. The grain on the right has been tilted to the [110] zone-axis; at this orientation the lattice planes for the left grain are not resolved. Figure 3b shows the Te:Cd core loss EELS intensity ratio mapped over the box region in Figure 3a. The grain boundary is Te-deficient, consistent with previous reports [29]. The Te:Cd intensity ratio profile across the grain boundary was extracted from an area close to the box region in Figure 3b and is plotted in Figure 3c. The Te:Cd intensity ratio decreases by ~9% over a 7.4 nm region across the grain boundary. Any chlorine segregation to the grain boundary from the chlorine activation process [5, 29] was below the detection limit of core loss EELS.

The Fourier-log deconvolved EELS single scattering distribution for bulk CdTe and grain boundary are shown superimposed in Figure 4a. The bulk CdTe spectrum was averaged from spectra extracted from within the left and right hand grains 20 nm away from the grain boundary (the two spectra were however nearly identical). The grain boundary spectrum was extracted from the box region in Figure 3b. Inelastic delocalisation is again an important artefact. This is evident from the simulated spectrum [25-26], also shown in Figure 4a, for a 4 nm grain boundary 'layer' sandwiched between two bulk CdTe grains. The dielectric constants extracted from low loss EELS measurements of bulk CdTe and grain boundary were used in the simulations; a grain boundary layer thickness of 4 nm was chosen since this corresponds to the full width at half maximum of the Te:Cd intensity ratio profile in Figure 3c. Due to delocalisation the simulated and measured grain boundary spectra do not exactly agree for the energy loss range ($\leq$ 4 eV) important for solar cell device operation. However, delocalisation is not significant for the doublet 'A' peak at ~13 eV, and this shows a decrease at the grain boundary compared to grain interior (Figure 4a).

Figures 4b and 4c show the real and imaginary parts of the complex dielectric function extracted from Kramers-Kronig analysis of the bulk CdTe and grain boundary EELS spectra in Figure 4a. The E_1, $E_1+\Delta_1$ and E_2 direct optical transitions are slightly suppressed at the grain boundary (Figure 4c). The effect this has on the optical absorption coefficient is however negligible, as can be seen from Figure 4d. Ideally the absorption coefficient at the grain boundary should be as small as possible, so that the incident light generates fewer charge carriers that are potentially lost to non-radiative recombination. The grain boundary analysed

here has a large misorientation to induce significant structural as well as chemical (i.e. Te-depletion) changes locally, but to within the measurement accuracy imposed by delocalisation, the change in absorption coefficient over solar spectrum wavelengths is small. In fact the largest change in absorption coefficient is only observed at much higher energies (~9 eV). Results for a different high angle grain boundary, which showed no Te-depletion, is presented in the Supplementary Information. This grain boundary also displayed a decrease in the doublet 'A' peak at ~13 eV with respect to bulk CdTe, although the changes to the absorption coefficient over solar spectrum wavelengths was small. The trend is therefore similar to the grain boundary in Figure 3a, despite the differences in Te composition at the two boundaries.

Gold back contact

Figure 5a is a HAADF image of the gold back contact; the Pt layer above the gold was deposited as a protective layer during FIB TEM sample preparation. The Au layer is ~50 nm thick and has noticeable surface roughness due to the underlying grain structure of the film, particularly at the interface with CdTe. Figure 5b shows the low loss EELS spectrum acquired from the middle of the Au back contact layer, where a peak is observed at ~2.7 eV. The simulated EELS spectrum for bulk Au is shown in Figure 5c and was calculated in the retarded regime using the optical constants listed in reference [30]. The overall shape of the simulated spectrum is similar to the experimental result in Figure 5b, although there are subtle differences, such as the 2.7 eV peak appearing at 2.5 eV, as well as higher intensity at energy losses between 1-2 eV for the experimental spectrum. These differences are possibly due to the fact that the measurements were performed on a Au layer sandwiched between Pt and CdTe in a thin TEM sample, so that additional surface and/or interface losses may be present, but are nevertheless not taken into account in the simulation. The 2.5 eV peak in Figure 5c is due to interband transitions in gold [30].

The low loss EELS spectrum extracted from the Au-CdTe interface (box region in Figure 5a) is also shown in Figure 5b. The 2.7 eV peak for the Au layer is now broader and is also red shifted, suggesting the presence of an additional interface loss contribution at lower energy. The non-retarded surface plasmon energy at the Au-CdTe boundary is determined by the zero crossing of the real part of $(\varepsilon_{Au} + \varepsilon_{CdTe})$, while the imaginary part must be close to zero to minimise plasmon damping [30]; for simplicity the finite thickness of the Au layer is not taken into account. In calculating $(\varepsilon_{Au} + \varepsilon_{CdTe})$ the dielectric constant in [30] for bulk Au was used for ε_{Au} and the experimental values for CdTe from this work was used for ε_{CdTe}. Figure 5d plots the real and imaginary parts of $(\varepsilon_{Au} + \varepsilon_{CdTe})$. A zero crossing is observed at 2 eV for the real part, and the imaginary part is also comparatively small in this energy range. This suggests that the red shift and broadening of the 2.7 eV peak at the Au-CdTe interface is due to surface plasmons at this boundary.

Radiative decay of surface plasmon polaritons (SPP) in noble metal nanoparticles has previously been used to enhance the photocurrent extracted from silicon solar cells [32-33]. For a perfectly flat Au-CdTe interface the surface plasmon is non-radiative, since its phase velocity is smaller than the speed of light in CdTe [31]. However, when the interface is rough, such as in a real device (Figure 5a), momentum can be transferred to the surface plasmon, thereby making it radiative [34-35]. This means that in a solar cell device the light incident

from the CdTe side can generate SPPs that propagate along the Au-CdTe interface before radiatively decaying into a photon that is backscattered into the CdTe. This is a potentially useful method for enhancing the photocurrent from photons with energy slightly above the band gap of CdTe. In a conventional device absorption of these low energy photons generate charge carriers deep within the CdTe layer, so that they are prone to surface recombination from the Au back contact or else recombine before diffusing to the space charge region. If the incident light can be backscattered via SPPs however the charge carriers will be generated closer to the space charge region, thereby increasing the photocurrent.

The maximum photocurrent gain achievable through the SPP backscattering mechanism is calculated and the results are shown in Figure 6. It is assumed that all photons incident at the Au-CdTe interface are backscattered and re-absorbed within the 2.5 μm thick CdTe layer. Furthermore, it is assumed that the charge carriers thus generated are fully extracted by the built-in electric field of the device. The photocurrent gain is calculated for photons above the CdTe band gap (1.5 eV or 827 nm) up to the non-retarded surface plasmon energy (2 eV or 620 nm). This energy range takes into account the dispersion in surface plasmon energy [31] as well as those photons that can be absorbed by CdTe. As expected the largest gain in photocurrent is for wavelengths close to the absorption threshold of CdTe. The total photocurrent gain that can be achieved for all wavelengths through the SPP mechanism is 2.4 mA/cm^2. This is ~13% of the calculated J_{sc} value (i.e. 18.1 mA/cm^2) and highlights the potential of the method. Nevertheless questions remain on the efficiency of SPP excitation by light and subsequent radiative decay, the ideal surface roughness of the Au back contact and ideal thickness of CdTe absorber layer. A more in-depth analysis is required to investigate these factors further.

Conclusions

Aberration corrected and monochromated STEM EELS is used to measure the local optical properties of interfaces in CdTe thin-film solar cells. Delocalisation in inelastic scattering was found to be a limiting factor in the accuracy of such high spatial resolution measurements. The dielectric function measured for the $CdTe_{1-x}S_x$ inter-diffusion layer at the CdS-CdTe interface indicated a smaller band gap, but a lower optical absorption coefficient over much of the solar spectrum range. The reflectivity of light at the CdS-$CdTe_{1-x}S_x$ interface is however better than CdS-CdTe. The benefits of improved reflectivity on the photocurrent is therefore offset by the lower absorption coefficient, resulting in only a modest change in J_{sc}. Sulphur inter-mixing has previously been identified as a contributing factor to J_{sc} losses, but this effect is not observed here. This could be due to systematic errors in the data arising from delocalisation artefacts, as well as the unknown effects of sulphur alloying on materials parameters (i.e. carrier diffusion length, doping concentration etc).

Subtle variations in optical transitions are also observed at CdTe grain boundaries, which are due to the abrupt change in the structure and/or chemistry (e.g. Te-depletion) at the grain boundary. However, this gives rise to only minor changes in the absorption coefficient in the visible or near-visible spectrum range at the grain boundary compared to the grain interior. Ideally the grain boundary should have a low absorption coefficient, so that any charge carriers generated by light absorption are not lost to non-radiative recombination via band gap defect

states. However, the results here suggest that grain boundaries in CdTe do not have a significant impact on the carrier generation profile within the absorber layer.

Measurements at the Au back contact-CdTe interface revealed a surface plasmon at ~2 eV. The Au layer is not smooth due to the underlying grain structure, and this surface roughness can cause the surface plasmon to couple with an electromagnetic field. Light incident from the CdTe side can therefore excite surface plasmon polaritons (SPP) at the Au-CdTe interface, which subsequently backscatter the light into the CdTe through radiative decay. This has the potential to increase the photocurrent for light wavelengths close to the absorption threshold of CdTe. Surface nano-patterning of $Cu(In,Ga)Se_2$ thin-film solar cells with water soluble KF salts has previously been used to create passivating layers with point contacts [36]. Similar surface treatments of CdTe could potentially be used to create the ideal surface roughness for promoting the SPP effect.

Acknowledgements

SuperSTEM is the UK Engineering and Physical Sciences Research Council (EPSRC) National Facility for Advanced Electron Microscopy and is funded under grant NS/A000057/1.

Figure Captions

Figure 1: (a) MAADF image of the CdS-CdTe interface. (b) EELS single scattering distributions for CdS, CdTe and the CdS-CdTe interface extracted from the box region in Figure 1a. The inset shows the energy loss onset for the three spectra. (c) shows the CdS-CdTe interface spectrum and the multiple linear least squares (MLLS) fit using CdS, CdTe and a delocalised signal as the reference spectra. The delocalised signal has the form $Im\{-2/(\varepsilon_{CdTe}+\varepsilon_{CdS})\}$, where ε_{CdTe}, ε_{CdS} are the dielectric functions for CdS and CdTe respectively and 'Im' represents the imaginary part of a complex number. Also shown in Figure 1c is the simulated spectrum for a 2.8 nm $CdTe_{1-x}S_x$ layer sandwiched between bulk CdS and CdTe. Analytical expressions for a multilayer system [24-25] were used in the simulation. The area under the curves in Figure 1c is normalised for direct comparison. (d) shows the S:Cd and Te:Cd core loss EELS intensity ratio profiles across the CdS-CdTe interface, along with the MAADF intensity. The curves have been normalised for direct comparison.

Figure 2: (a) real (ε_1) and (b) imaginary (ε_2) parts of the complex dielectric function for the $CdTe_{1-x}S_x$ interface layer and bulk CdTe, extracted from a Kramers-Kronig analysis of the EELS spectra in Figure 1b. The absorption coefficient (α) over solar spectrum wavelengths important for solar cell device operation is plotted in (c). (d) shows the reflectivity as a function of wavelength for a CdS-CdTe interface (labelled 'CdTe') and CdS-$CdTe_{1-x}S_x$ interface (labelled '$CdTe_{1-x}S_x$'). The simulated external quantum efficiency (EQE) for the CdS-CdTe and CdS-$CdTe_{1-x}S_x$ devices are plotted in (e).

Figure 3: (a) MAADF image of a high angle CdTe grain boundary. (b) shows the Te:Cd core loss EELS intensity ratio mapped over the box region in Figure 3a. The Te:Cd intensity ratio profile across the grain boundary is shown in (c). The profile was extracted from an area close

to the box region in Figure 3b. The average Te:Cd ratio for the grain interior on the right hand side has been normalised to unity.

Figure 4: (a) EELS single scattering distributions for bulk CdTe and CdTe grain boundary are superimposed with the area under the curves normalised for direct comparison. The grain boundary spectrum was extracted from the box region in Figure 3b. Also shown in Figure 4a is the simulated spectrum for a 4 nm grain boundary 'layer' sandwiched between bulk CdTe. Analytical expressions for a multilayer system [24-25] were used in the simulation. The real (ε_1) and imaginary (ε_2) parts of the complex dielectric function for CdTe and CdTe grain boundary are shown in (b) and (c) respectively. The corresponding absorption coefficient (α) over solar spectrum wavelengths for solar cell device operation is plotted in (d).

Figure 5: (a) HAADF image of Au-CdTe interface. The Pt overlayer was deposited during FIB TEM specimen preparation. (b) Low loss EELS spectra for the Au layer and Au-CdTe interface. The latter was extracted from the box region in Figure 5a. The zero loss peak has not been subtracted from the individual spectra, although its intensity was normalised for a more direct comparison. (c) shows the low loss EELS spectrum for bulk gold simulated in the retarded regime. The real and imaginary part of ($\varepsilon_{Au} + \varepsilon_{CdTe}$), where ε_{Au}, ε_{CdTe} are the dielectric functions for Au and CdTe respectively, is shown in (d).

Figure 6: Photocurrent gain as a function of wavelength of incident light for the surface plasmon polariton (SPP) mechanism in a 2.5 μm thick CdTe film with Au back contact. It is assumed that all the light incident on the Au layer is SPP backscattered and re-absorbed within the CdTe to produce charge carriers with 100% collection efficiency.

References

[1] M.A. Green, Y. Hishikawa, W. Warta, E.D. Dunlop, D.H. Levi, J. Hohl-Ebinger, A.W.H. Ho-Baillie, Solar cell efficiency tables (version 51), *Prog. Photovolt: Res. Appl.* (2018) **26**, 3.

[2] N.R. Paudel, Y. Yan, Enhancing the photo-currents of CdTe thin-film solar cells in both short and long wavelength regions, *Appl. Phys. Lett.* (2014) **105**, 183510.

[3] J.D. Poplawsky, W. Guo, N. Paudel, A. Ng, K. More, D. Leonard, Y. Yan, Structural and compositional dependence of the $CdTe_xSe_{1-x}$ alloy layer photoactivity in CdTe-based solar cells, *Nature Comms.* (2016) **7**, 12537.

[4] T. Baines, G. Zoppi, L. Bowen, T.P. Shalvey, S. Mariotti, K. Durose, J.D. Major, Incorporation of CdSe layers into CdTe thin film solar cells, *Sol. Energy Mat. Sol. Cells* (2018) **180**, 196.

[5] M. Terheggen, H. Heinrich, G. Kostorz, A. Romeo, D. Bätzner, A.N. Tiwari, A. Bosio, N. Romeo, Structural and chemical interface characterisation of CdTe solar cells by transmission electron microscopy, *Thin Solid Films* (2003) **431-432**, 262.

[6] A.A. Taylor, J.D. Major, G. Kartopu, D. Lamb, J. Duenow, R.G. Dhere, X. Maeder, S.J.C. Irvine, K. Durose, B.G. Mendis, A comparative study of microstructural stability and sulphur diffusion in CdS/CdTe photovoltaic devices, *Sol. Energy Mat. Sol. Cells* (2015) **141**, 341.

[7] S.H. Demtsu, J.R. Sites, Quantification of losses in thin-film CdS/CdTe solar cells, *Proceedings of the 31st IEEE Photovoltaic Specialist Conference* (2005) p. 347.

[8] O.L. Krivanek, J.P. Ursin, N.J. Bacon, G.J. Corbin, N. Delby, P. Hrncirik, M.F. Murfitt, C.S. Own, Z.S. Szilagyi, High energy resolution monochromator for aberration corrected scanning transmission electron microscopy/electron energy loss spectroscopy, *Phil. Trans. R. Soc. A* (2009) **367**, 3683.

[9] R.F. Egerton, *Electron Energy Loss Spectroscopy in the Electron Microscope*, Second Edition (1996), Plenum Press, New York.

[10] M. Stöger-Pollach, Optical properties and band gaps from low loss EELS: pitfalls and solutions, *Micron* (2008) **39**, 1092.

[11] M. Stöger-Pollach, P. Schattschneider, The influence of relativistic energy losses on bandgap determination using valence EELS, *Ultramicroscopy* (2007) **107**, 1178.

[12] D.A. Muller, J. Silcox, Delocalisation in inelastic scattering, *Ultramicroscopy* (1995) **59**, 195.

[13] J.D. Major, Y.Y. Proskuryakov, K. Durose, G. Zoppi, I. Forbes, Control of grain size in sublimation-grown CdTe, and the improvement in performance of devices with systematically increased grain size, *Sol. Energy Mat. Sol. Cells* (2010) **94**, 1107.

[14] B.G. Mendis, L. Bowen, Q.Z. Jiang, A contactless method for measuring the recombination velocity of an individual grain boundary in thin-film photovoltaics, *Appl. Phys. Lett.* (2010) **97**, 092112.

[15] B.G. Mendis, D. Gachet, J.D. Major, K. Durose, Long lifetime hole traps at grain boundaries in CdTe thin-film photovoltaics, *Phys. Rev. Lett.* (2015) **115**, 218701.

[16] J.D. Major, Y.Y. Proskuryakov, K. Durose, Impact of CdTe surface composition on doping and device performance in close space sublimation deposited CdTe solar cells, *Prog. Photovolt: Res. Appl.* (2013) **21**, 436.

[17] J.D. Major, R.E. Treharne, L.J. Phillips, K. Durose, A low cost non-toxic post-growth activation step for CdTe solar cells, *Nature* (2014) **511**, 334.

[18] J.A. Alexander, F.J. Scheltens, L.F. Drummy, M.F. Durstock, F.S. Hage, Q.M. Ramasse, D.W. McComb, High resolution monochromated electron energy loss spectroscopy of organic photovoltaic materials, *Ultramicroscopy* (2017) **180**, 125.

[19] R. Erni, N.D. Browning, The impact of surface and retardation losses on valence electron energy loss spectroscopy, *Ultramicroscopy* (2008) **108**, 84.

[20] D.A. Wood, K.D. Rogers, D.W. Lane, J.A. Coath, Optical and structural characterisation of CdS_xTe_{1-x} thin films for solar cell applications, *J. Phys: Condens. Matter* (2000) **12**, 4433.

[21] D.A. Wood, K.D. Rogers, D.W. Lane, G.J. Conibeer, D. Parton, A study of the phase boundaries and lattice parameters of the CdS-CdTe pseudobinary system, *J. Mat. Sci. Lett.* (1998) **17**, 1511.

[22] B. Rafferty, L.M. Brown, Direct and indirect transitions in the region of the band gap using electron energy loss spectroscopy, *Phys. Rev. B* (1998) **58**, 10326.

[23] H. Dröge, A. Fleszar, W. Hanke, M. Sing, M. Knupfer, J. Fink, F. Goschenhofer, C.R. Becker, R. Kargerbauer, H.P. Steinrück, Complex loss function of CdTe, *Phys. Rev. B* (1999) **59**, 5544.

[24] Z.L. Wang, Valence electron excitations and plasmon oscillations in thin films, surfaces, interfaces, and small particles, *Micron* (1996) **27**, 265.

[25] J.P.R. Bolton, M. Chen, Electron energy loss in multi-layered slabs, *Ultramicroscopy* (1995) **60**, 247.

[26] J.P.R. Bolton, M. Chen, Electron energy loss in multi-layered slabs: I. Normal incidence, *J. Phys.: Condens. Matter* (1995) **7**, 3373.

[27] S. Adachi, T. Kimura, N. Suzuki, Optical properties of CdTe: Experiment and modelling, *J. Appl. Phys.* (1993) **74**, 3435.

[28] B.G. Mendis, R.E. Treharne, D.W. Lane and K. Durose, The effects of junction interdiffusion and misfit dislocations on the efficiency of highly mismatched heterojunction photovoltaic devices, *Appl. Phys. Lett.* (2016) **108**, 183505.

[29] C. Li, J. Poplawsky, Y. Wu, A.R. Lupini, A. Mouti, D.N. Leonard, N. Paudel, K. Jones, W. Yin, M. Al-Jassim, Y. Yan, S.J. Pennycook, From atomic structure to photovoltaic properties in CdTe solar cells, *Ultramicroscopy* (2013) **134**, 113.

[30] P.B. Johnson, R.W. Christy, Optical constants of the noble metals, *Phys. Rev. B* (1972) **6**, 4370.

[31] J.M. Pitarke, V.M. Silkin, E.V. Chulkov, P.M. Echenique, Theory of surface plasmons and surface-plasmon polaritons, *Rep. Prog. Phys.* (2007) **70**, 1.

[32] S. Pillai, K.R.Catchpole, T.Trupke, M.A. Green, Surface plasmon enhanced silicon solar cells, *J. Appl. Phys.* (2007) **101**, 093105.

[33] T.L. Temple, G.D.K. Mahanama, H.S. Reehal, D.M. Bagnall, Influence of localised surface plasmon excitation in silver nanoparticles on the performance of silicon solar cells, *Sol. Energy Mat. Sol. Cells* (2009) **93**, 1978.

[34] Y.Y. Teng, E.A. Stern, Plasma radiation from metal grating surfaces, *Phys. Rev. Lett.* (1967) **19**, 511.

[35] M. Kuttge, E.J.R. Vesseur, A.F. Koenderink, H.J. Lezec, H.A. Atwater, F.J. Garcia de Abajo, A. Polman, Local density of states, spectrum, and far-field interference of surface plasmon polaritons probed by cathodoluminescence, *Phys. Rev. B* (2009) **79**, 113405.

[36]. P. Reinhard, B. Bissig, F. Pianezzi, H. Hagendorfer, G. Sozzi, R. Menozzi, C. Gretener, S. Nishiwaki, S. Buecheler, A.N. Tiwari, Alkali-templated surface nano-patterning of chalcogenide thin-films: a novel approach toward solar cells with enhanced efficiency, *Nano Lett.* (2015) **15**, 3334.

Figures

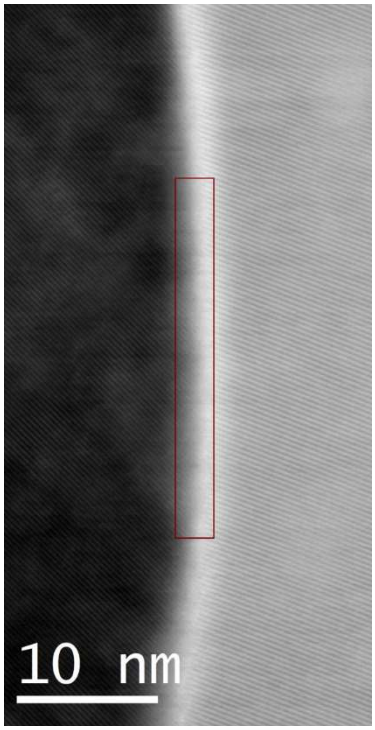
10 nm

(a)

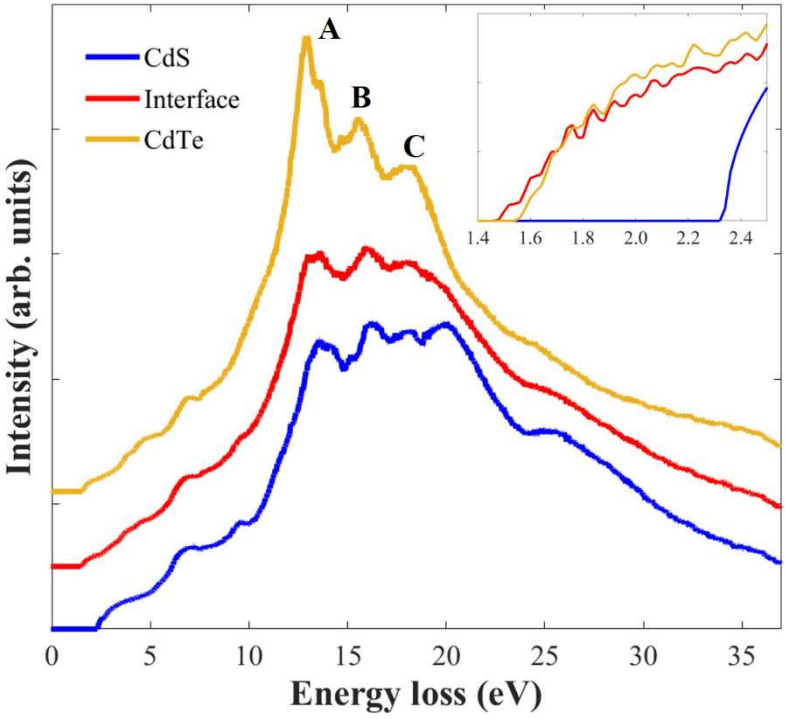
CdS
Interface
CdTe
A
B
C
Intensity (arb. units)
Energy loss (eV)
0
5
10
15
20
25
30
35
1.4
1.6
1.8
2.0
2.2
2.4

(b)

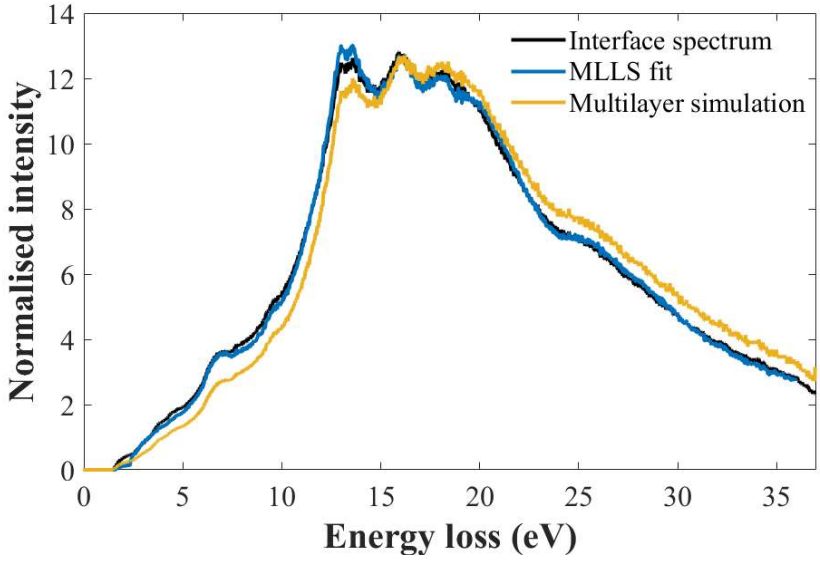
Interface spectrum
MLLS fit
Multilayer simulation
Normalised intensity
Energy loss (eV)
0
2
4
6
8
10
12
14
0
5
10
15
20
25
30
35

(c)

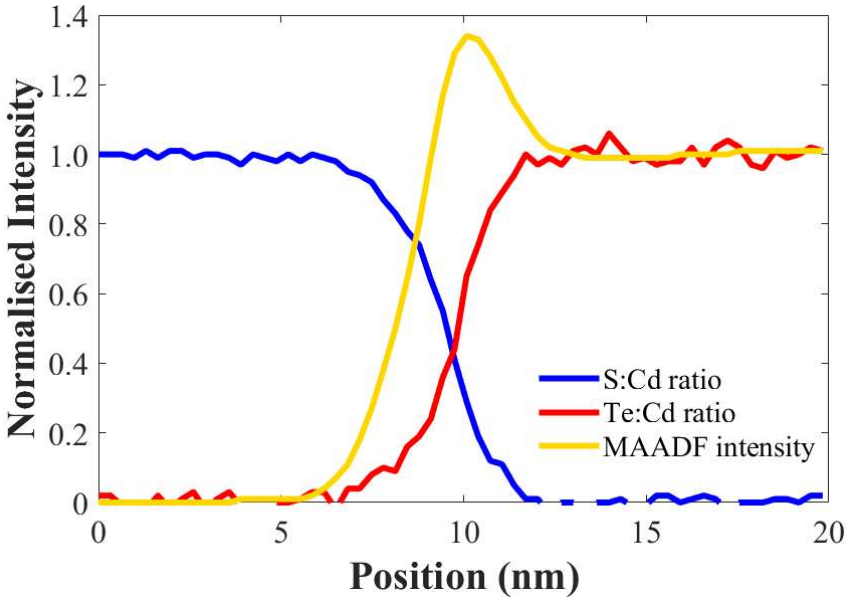
S:Cd ratio
Te:Cd ratio
MAADF intensity
Normalised Intensity
Position (nm)
0
0.2
0.4
0.6
0.8
1.0
1.2
1.4
0
5
10
15
20

(d)

Figure1

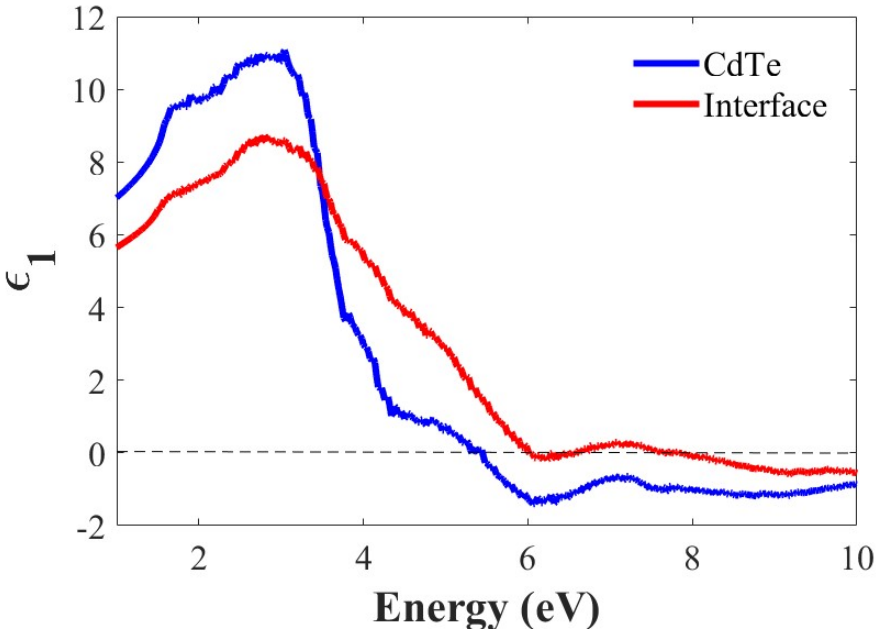
CdTe
Interface
ϵ_1
Energy (eV)

(a)

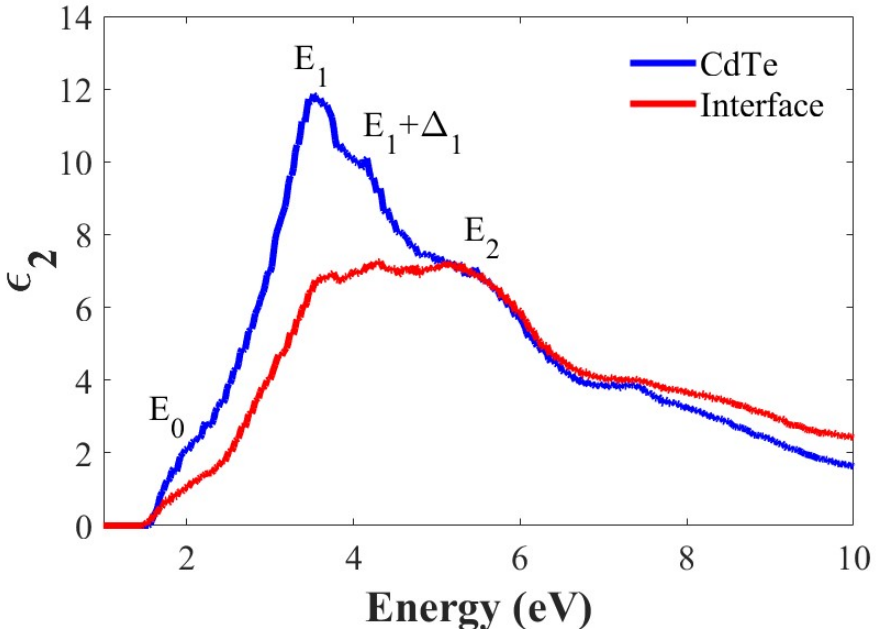
CdTe
Interface
E_0
E_1
$E_1+\Delta_1$
E_2
ϵ_2
Energy (eV)

(b)

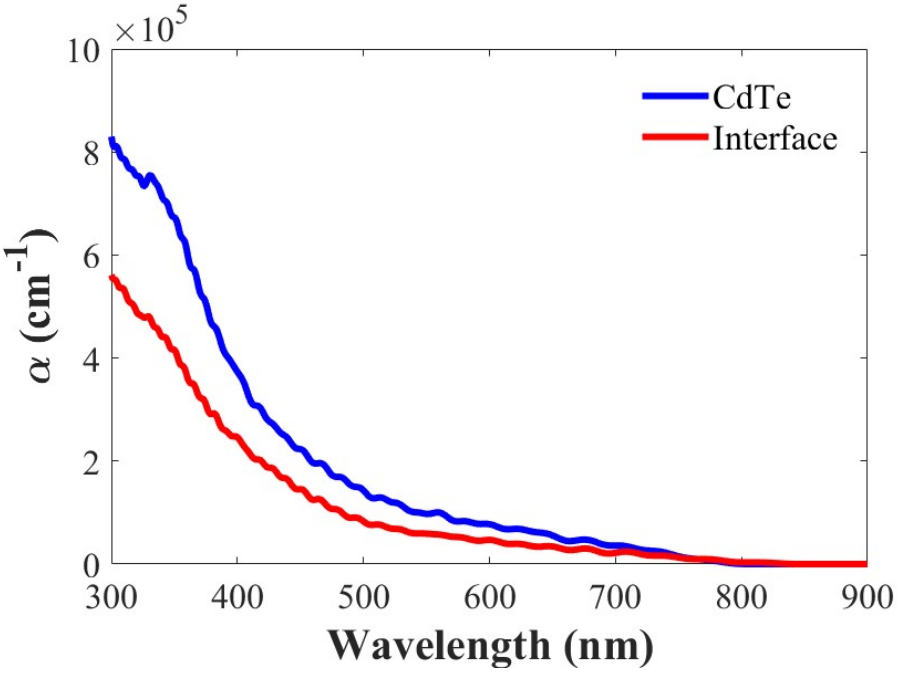
×10^5
10
8
6
4
2
0
α (cm^-1)
CdTe
Interface
300
400
500
600
700
800
900
Wavelength (nm)

(c)

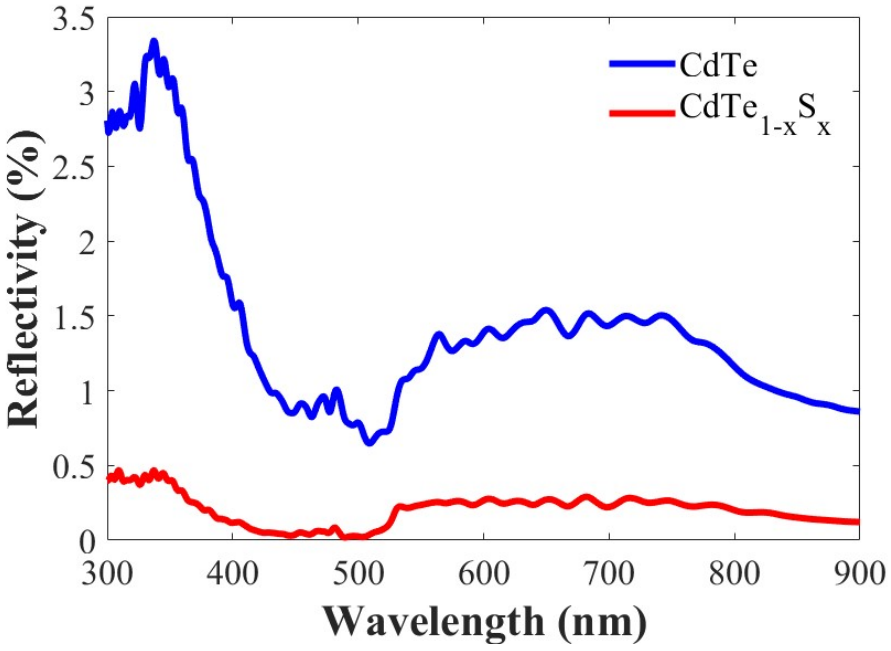
3.5
3
2.5
2
1.5
1
0.5
0
Reflectivity (%)
CdTe
CdTe1-xSx
300
400
500
600
700
800
900
Wavelength (nm)

(d)

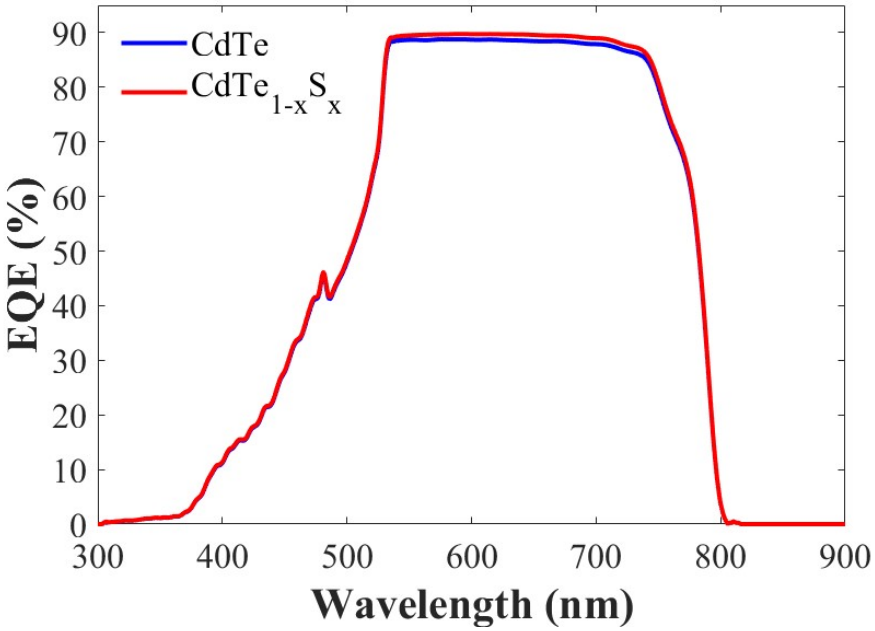
CdTe
CdTe1-xSx
EQE (%)
Wavelength (nm)
0
10
20
30
40
50
60
70
80
90
300
400
500
600
700
800
900

(e)

Figure 2

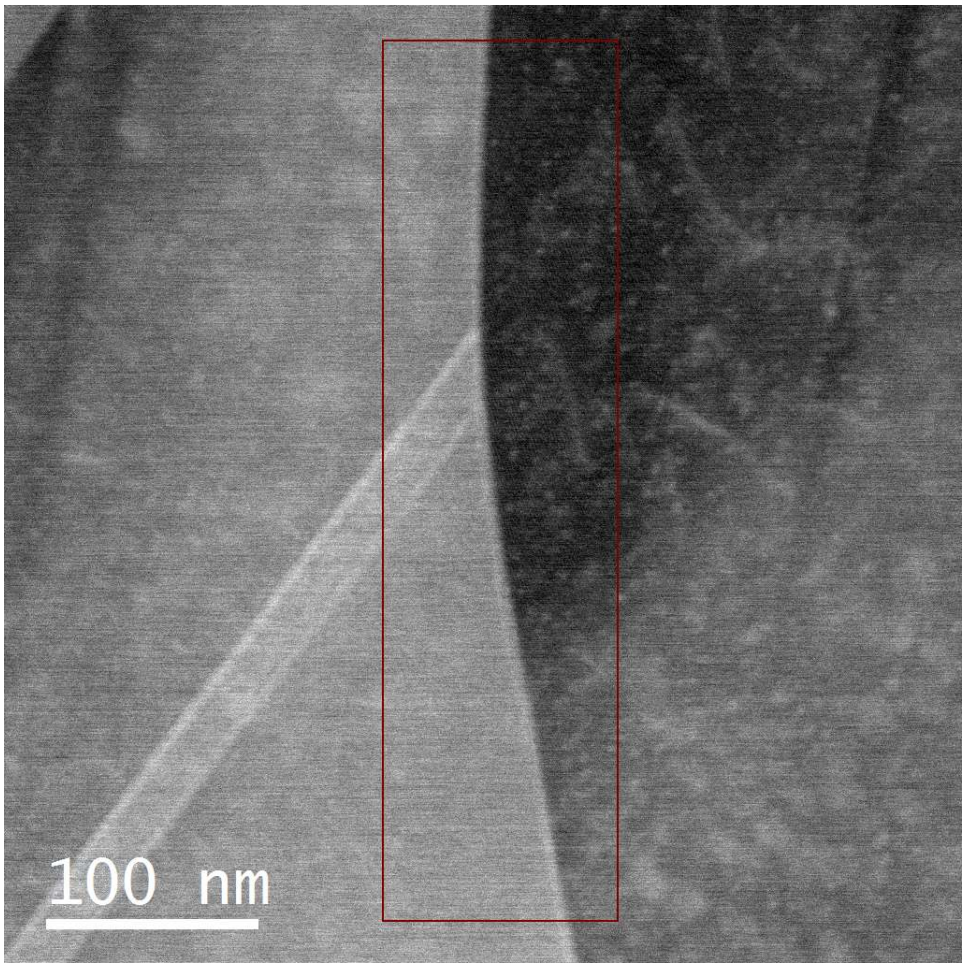
100 nm

(a)


50 nm

(b)

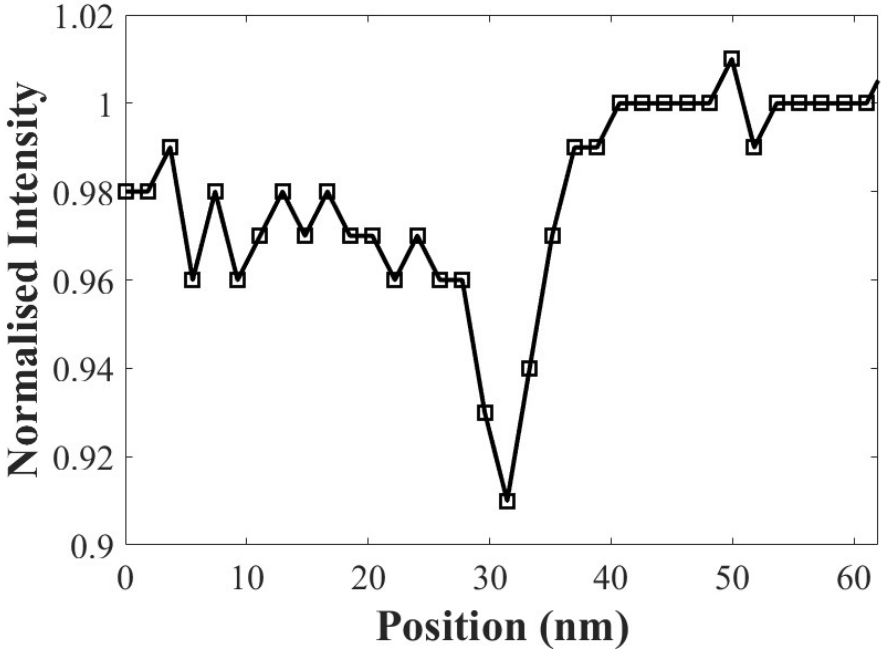
Normalised Intensity
1.02
1
0.98
0.96
0.94
0.92
0.9
0
10
20
30
40
50
60
Position (nm)

(c)

Figure 3

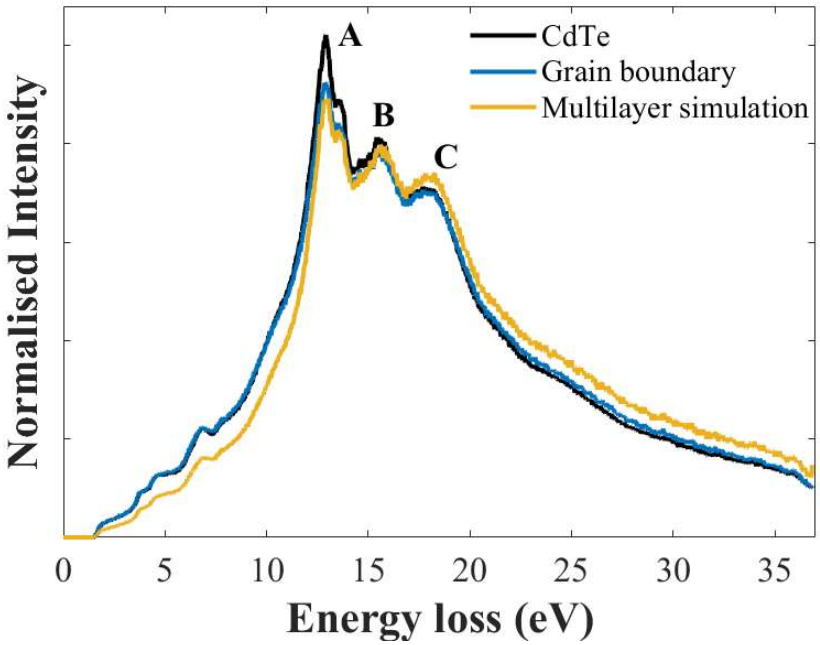
A
B
C
CdTe
Grain boundary
Multilayer simulation
Normalised Intensity
0
5
10
15
20
25
30
35
Energy loss (eV)

(a)

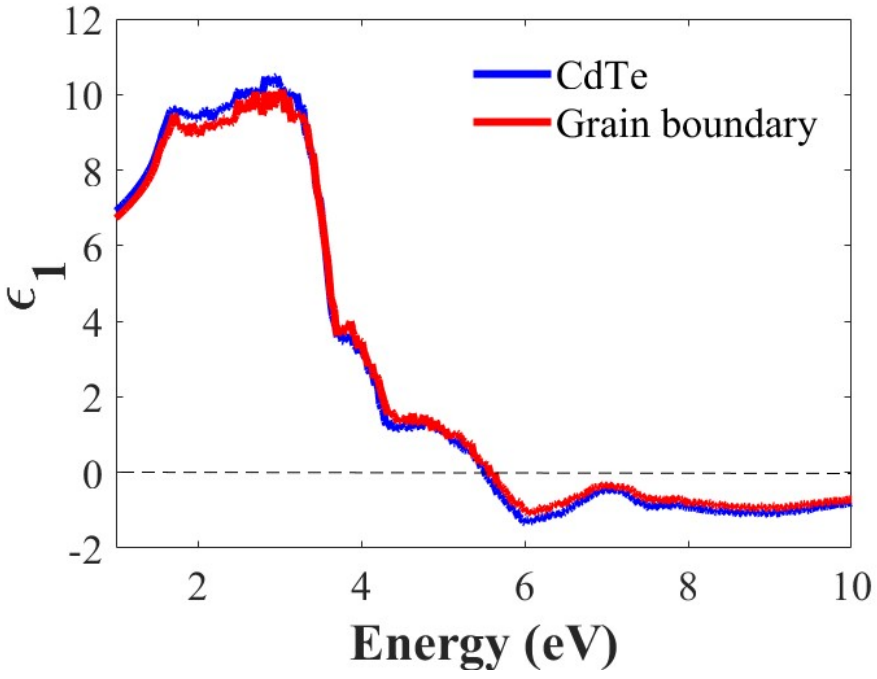
CdTe
Grain boundary
ϵ_1
12
10
8
6
4
2
0
-2
2
4
6
8
10
Energy (eV)

(b)

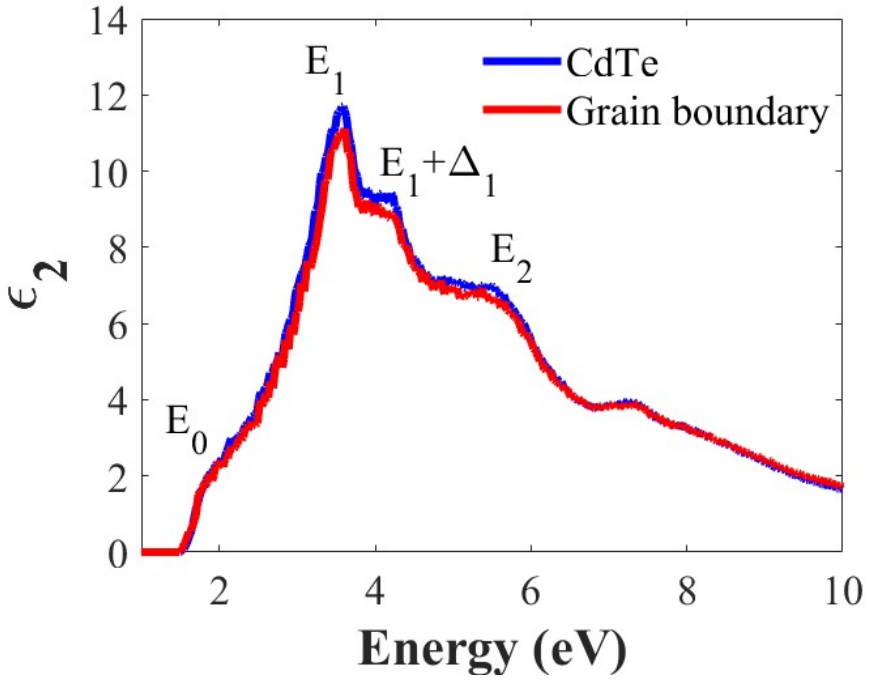
14
12
10
8
6
4
2
0
ϵ_2
E_1
$E_1+\Delta_1$
E_2
E_0
CdTe
Grain boundary
2
4
6
8
10
Energy (eV)

(c)

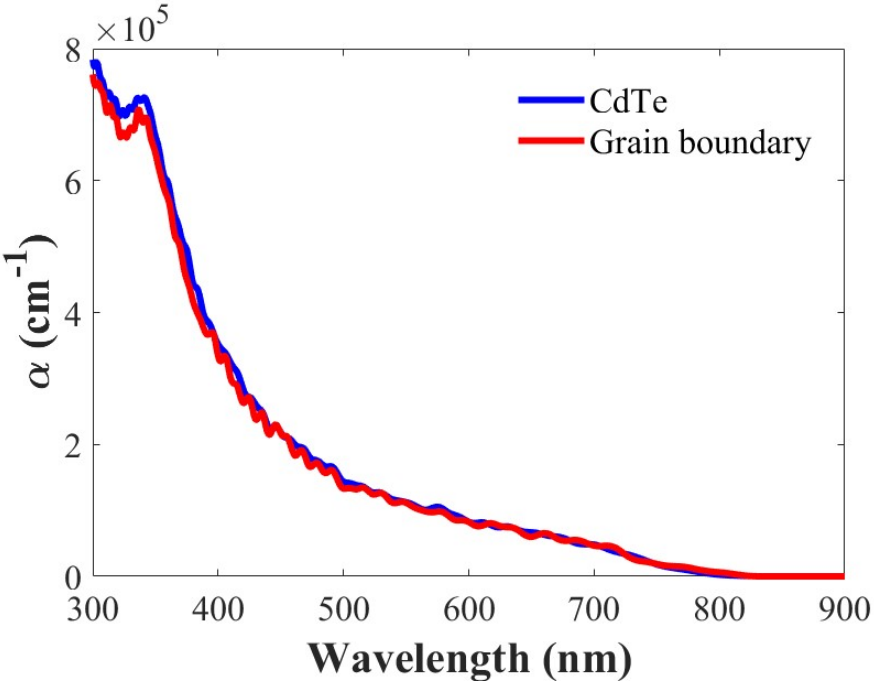
$\times 10^5$
8
6
4
2
0
α (cm^{-1})
CdTe
Grain boundary
300
400
500
600
700
800
900
Wavelength (nm)

(d)

Figure 4

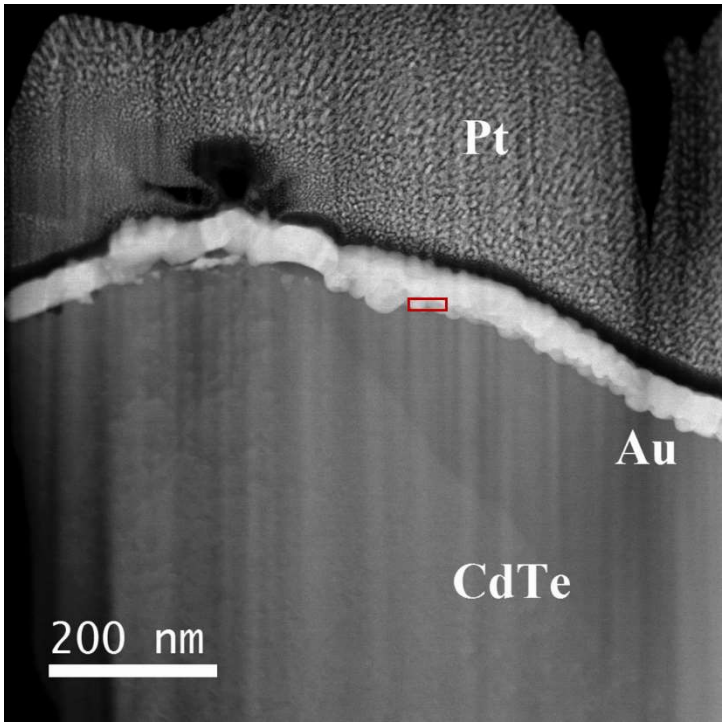
Pt
Au
CdTe
200 nm

(a)

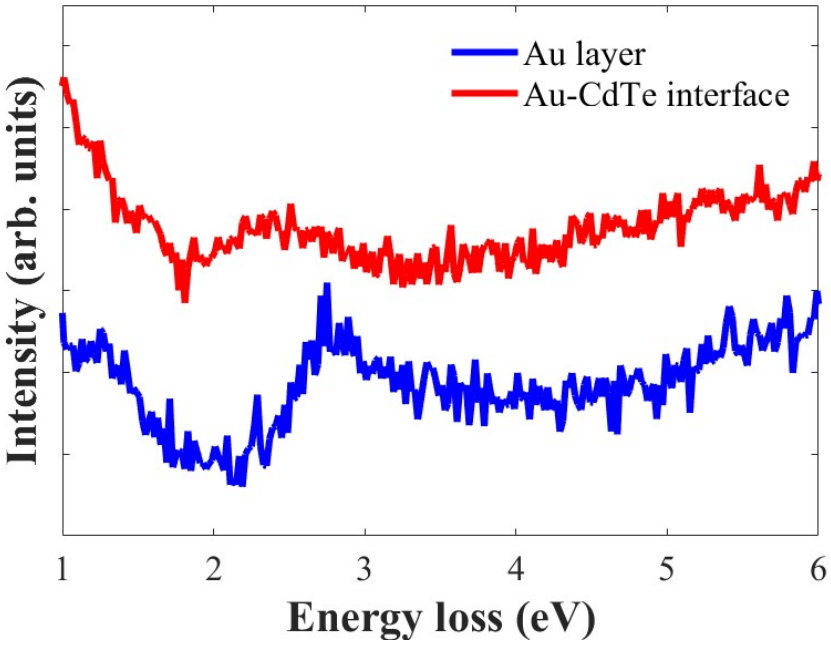
Au layer
Au-CdTe interface
Intensity (arb. units)
1
2
3
4
5
6
Energy loss (eV)

(b)

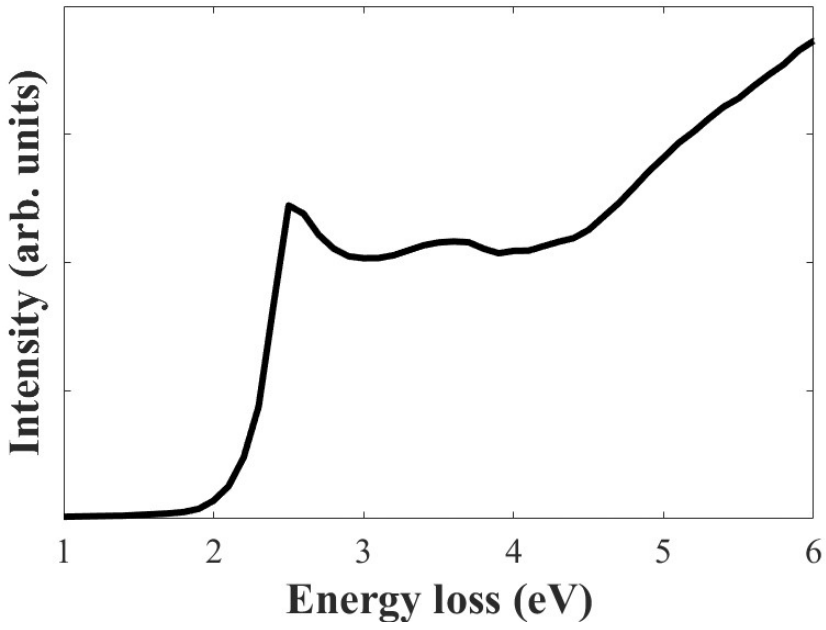
Intensity (arb. units)
1
2
3
4
5
6
Energy loss (eV)

(c)

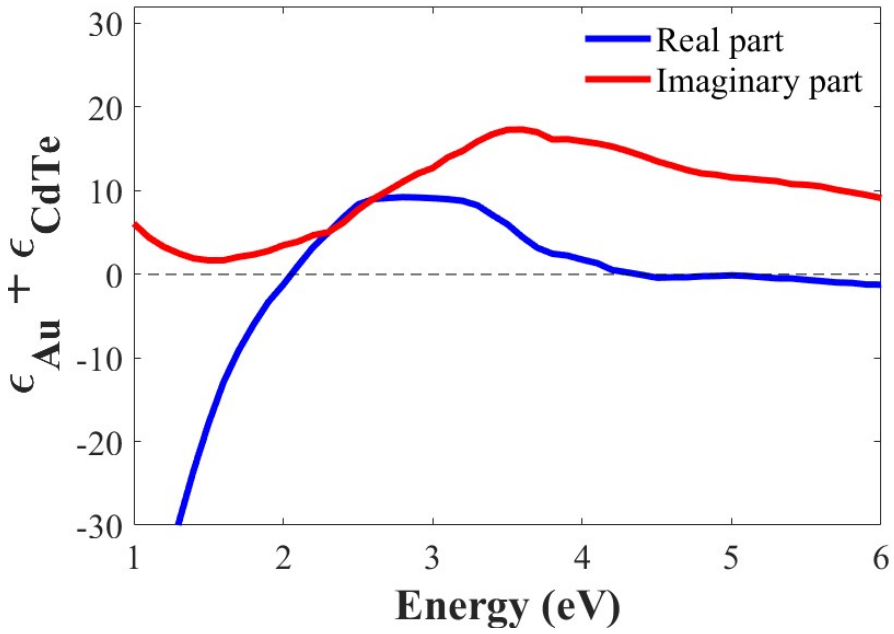
Real part
Imaginary part
30
20
10
0
-10
-20
-30
$\epsilon_{Au} + \epsilon_{CdTe}$
1
2
3
4
5
6
Energy (eV)

(d)

Figure 5

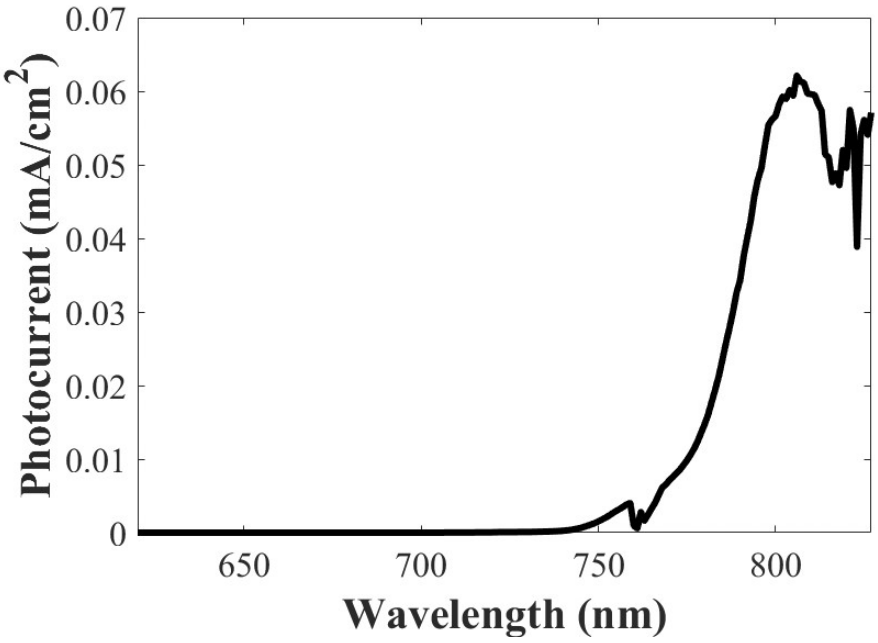
0.07
0.06
0.05
0.04
0.03
0.02
0.01
0
Photocurrent (mA/cm2)
650
700
750
800
Wavelength (nm)

Figure 6